PNAS RESEARCH ARTICLE | MICROBIOLOGY

Proton transfer activity of the reconstituted *Mycobacterium tuberculosis* MmpL3 is modulated by substrate mimics and inhibitors

Casey M. Stevens[a], Svitlana O. Babii[a], Amitkumar N. Pandya[b], Wei Li[c], Yupeng Li[d,e,f], Jitender Mehla[a], Robyn Scott[b], Pooja Hegde[b], Pavan K. Prathipati[b], Atanu Acharya[f], Jinchan Liu[d,e,f], James C. Gumbart[f], Jeffrey North[b], Mary Jackson[c], and Helen I. Zgurskaya[a,1]

Edited by Oren Rosenberg, University of California, San Francisco, CA; received August 2, 2021; accepted June 3, 2022 by Editorial Board Member Carl F. Nathan

Transporters belonging to the Resistance-Nodulation-cell Division (RND) superfamily of proteins such as *Mycobacterium tuberculosis* MmpL3 and its analogs are the focus of intense investigations due to their importance in the physiology of *Corynebacterium–Mycobacterium–Nocardia* species and antimycobacterial drug discovery. These transporters deliver trehalose monomycolates, the precursors of major lipids of the outer membrane, to the periplasm by a proton motive force–dependent mechanism. In this study, we successfully purified, from native membranes, the full-length and the C-terminal truncated *M. tuberculosis* MmpL3 and *Corynebacterium glutamicum* CmpL1 proteins and reconstituted them into proteoliposomes. We also generated a series of substrate mimics and inhibitors specific to these transporters, analyzed their activities in the reconstituted proteoliposomes, and carried out molecular dynamics simulations of the model MmpL3 transporter at different pH. We found that all reconstituted proteins facilitate proton translocation across a phospholipid bilayer, but MmpL3 and CmpL1 differ dramatically in their responses to pH and interactions with substrate mimics and indole-2-carboxamide inhibitors. Our results further suggest that some inhibitors abolish the transport activity of MmpL3 and CmpL1 by inhibition of proton translocation.

tuberculosis | drug target | membrane transporter | reconstitution

Mycobacterium tuberculosis (*Mtb*), the causative agent of tuberculosis, remains the leading cause of infectious disease worldwide, affecting approximately a quarter of the globe's population (1). Treatment of *Mtb* infections is problematic because of the emergence of multidrug- and extensively drug-resistant strains. The persistence of the infection, and the intrinsic resistance of *Mtb* to antibiotics, necessitates the use of long-term combination therapy (1).

Mtb is a member of the *Corynebacterium–Mycobacterium–Nocardia* (CMN) family of gram-positive, mycolic acid–containing bacteria. While many members of this bacterial family are ubiquitous in the environment and benign, the pathogenic members of this family cause some of the most widespread and difficult to treat human infections (2). While *Mtb* is the most well-known and studied pathogen of the family (3), the CMN family also contains *Mycobacterium leprae,* the causative agent of human leprosy, as well as *Mycobacterium abscessus* and *Mycobacterium avium.* The latter two are classified as emerging agents of nontubercular mycobacterial (NTM) infections (4) and are notoriously difficult to treat, due to their intrinsic resistance and ability to colonize bodily regions with poor therapeutic permeation (5). *Nocardia asteroides* can cause nocardiosis in immunocompromised individuals, a severe pulmonary infection similar in nature to tuberculosis (6). *Corynebacterium diphtheria* was the initial agent of the disease diphtheria, however *Corynebacterium ulcerans* has also been demonstrated to produce the diphtheria toxin and is therefore another causative agent of the disease (7).

A defining biochemical feature of the members of the CMN family is the synthesis of mycolic acids. Mycolic acids are long-chain fatty acids synthesized inside the bacterial cell and then transported across the cell membrane into the periplasm in the form of trehalose monomycolate (TMM) where mycolyltransferases of the antigen 85 family transfer the mycolic acid chain onto the nonreducing arabinan termini of the heteropolysaccharide, arabinogalactan (8, 9). Additionally, the antigen 85 complex proteins (Ag85A/B/C) catalyze the transesterification of two TMM molecules to form trehalose dimycolate (TDM) (10). The arabinogalactan-linked mycolic acids form the inner leaflet of the outer mycomembrane, while the TDM participates in the formation of the outer leaflet. This outer mycomembrane presents an amazingly effective barrier to drug

Significance

The *Corynebacterium–Mycobacterium–Nocardia* family of gram-positive, mycolic acid–containing bacteria is ubiquitous in the environment, and its pathogenic members cause some of the most widespread and difficult to treat infectious diseases. Mycobacterial and corynebacterial transporters of the MmpL/CmpL family are physiologically essential to these pathogens and are the targets of novel drug candidates. The mechanism of inhibition of these transporters remains unclear. We purified the MmpL3 and CmpL1 transporters in their functional states, reconstituted them into isolated phospholipid bilayers, and analyzed how substrate mimics and inhibitors affect their proton transport activities. Our study provides a biochemical foundation for understanding the mechanism of these transporters and their inhibition by small molecules that will facilitate the development of novel antibiotics.

The authors declare no competing interest.

This article is a PNAS Direct Submission. O.R. is a guest editor invited by the Editorial Board.

See online for related content such as Commentaries.

[1]To whom correspondence may be addressed. Email: elenaz@ou.edu.

This article contains supporting information online at http://www.pnas.org/lookup/suppl/doi:10.1073/pnas.2113963119/-/DCSupplemental.

Published July 19, 2022.

entry (11, 12), and its proper biosynthesis and assembly are essential for cell viability. Accordingly, some of the most effective frontline medications available for mycobacterial infections target the biosynthesis of mycolic acids or other essential cell wall constituents (13).

The steps in the synthesis of mycolic acids have been well documented (8), starting with the biosynthesis of the 26-carbon saturated fatty acid (alpha chain) and the 56-carbon mostly saturated fatty tail (meromycolate), both of which are combined together by the condensase Pks13 (14, 15) along with a trehalose disaccharide forming immature ketomycolic acids esterified to trehalose. The latter may then undergo modification by the corynemycolate reductase CmrA (16, 17) to form the mature mycolic acids, and further modification via the addition of an acetyl group by the acetylase TmaT (18). However, the precise order of these reactions remains unclear. The acetylation of the mycolic motif appears to be a signal required for the mature TMM to be flipped from the inner leaflet of the cytoplasmic membrane to the outer leaflet by integral membrane transporters such as CmpL1 (Corynebacterial membrane protein Large 1) (19–21) and MmpL3 (21–24) (Mycobacterial membrane protein Large 3).

CmpL1/MmpL3 are members of the Resistance-Nodulation-Division (RND) superfamily of membrane transporters and are highly conserved among the CMN family of bacteria (19). Like other RND transporters, CmpL1/MmpL3 are large integral membrane proteins consisting of 12 transmembrane helices and two large periplasmic loops located between TMS 1/2 and TMS 7/8. A homotrimeric quaternary structure similar to that of gram-negative RND multidrug efflux pumps has been previously reported based on negative staining electron microscopy and homology modeling (20). In agreement, MmpL3 was found to be an oligomer in vivo, likely a trimer (20, 25, 26). Although its C-terminal domain is not required for function, it is needed for MmpL3 oligomerization and for localization of the protein to the cell division site (20, 26). More-recent structural studies suggested that these proteins might function as monomers, based on the crystal structures obtained from a C-terminal truncated *Mycobacterium smegmatis* MmpL3 protein and the cryoelectron microscopy structure of a C-terminal truncated *Mtb* MmpL3 (27–29). The biochemical mechanism of the transport reaction mediated by CmpL1/MmpL3 proteins remains unclear. A high degree of conservation of the proton translocation pathway among the RND family of transporters implies a proton:substrate antiport mechanism. A flippase-like mechanism, in which TMM is flipped from the inner to the outer leaflet of the cytoplasmic membrane, as well as an extrusion of TMM from the outer leaflet into the periplasm have been proposed, and both mechanisms have gained some experimental support (24).

In this study, we analyze the biochemical properties of MmpL3 from *Mtb* (MmpL3tb) and CmpL1 from *Corynebacterium glutamicum*. Unlike *Mtb*, which contains 13 RND transporters of which MmpL3tb is essential for viability, *C. glutamicum* contains only 4, with CmpL1 expendable if its CmpL4 homolog is present. CmpL1 and MmpL3tb share 43% identity and 63% similarity, and both are required for the transport of TMM to the cell surface. Their substrates, however, differ in length of hydrocarbon chains, with 22 to 26 carbons in coryne-TMM (TMCM) and up to 90 carbons in mycobacterial TMM. MmpL3tb and its homologs have been identified as novel and druggable therapeutic targets, as validated by in vitro studies (30, 31) as well as macrophage (32) and mouse infection models (33, 34). Screening large compound libraries for antibacterial compounds active against *Mtb* and emerging NTM pathogens identified several structurally diverse hits acting on MmpL3tb (23, 35–37). However, the specificity and molecular mechanism of action of these compounds are still under investigation.

Here, we use the similarities and differences between CmpL1 and MmpL3tb and structurally diverse inhibitors to gain insight into the mechanism of transport and inhibition of these transporters.

Results

MmpL3tb and CmpL1 Are Proton Motive Force–Driven Transporters. To characterize their biochemical properties, we purified the full-length MmpL3tb and CmpL1 proteins from *M. smegmatis* mc^2155 and *C. glutamicum* LY108, respectively (26, 38). In addition, we purified, from *Escherichia coli*, a monomeric MmpL3ΔCtb variant lacking the C-terminal domain, analogous to the protein constructs used in previous structural studies (27–29). To reconstitute these proteins into proteoliposomes, Triton X-100 was exchanged with octyl β-D-glucopyranoside, phospholipids were mixed with purified proteins, the detergent was diluted out, and the mix was dialyzed against biobeads to remove any residual detergent molecules. Control vesicles devoid of protein were prepared in parallel. We then tested whether the reconstituted MmpL3tb, MmpL3ΔCtb, and CmpL1 translocate protons, by following the intravesicular pH with the water-soluble fluorescent pH probe pyranine, which does not cross the vesicle membrane (Fig. 1) (39, 40). Pyranine was entrapped into protein-containing and empty vesicles by extrusion through filters with 200-nm pores, and the extravesicular pyranine was removed by gel filtration.

When protein-free vesicles with entrapped pyranine were preequilibrated in the pH 7.0 buffer and then were diluted into the pH 6.0 buffer or the pH 8.0 buffer, the pyranine fluorescence (therefore intravesicular pH) did not change significantly during the 5-min experiment, suggesting that spontaneous leakage of H^+ in the reconstituted vesicles was negligible (Fig. 2*A*). Upon addition of nigericin, which permeabilizes lipid bilayers to H^+, the pH gradient collapsed instantaneously (*SI Appendix*, Fig. S1). When a substrate analog **AcTre67** (Fig. 3*A*) containing a trehalose headgroup acylated with a 16-carbon-long tail (C16) was added to the vesicles at three different external pH, the lipid bilayer did not show significant changes in leakiness when compared to vesicles that were not exposed to **AcTre67** (Fig. 2*B*). **AcTre67** (0.05 μM) did not affect fluorescence when added directly to a solution of pyranine. The same results were obtained for other substrate mimetics of the MmpL3/CmpL1 pumps containing C4 (**AcTre246**), C10 (**AcTre243**), C12 (**AcTre244**), and C14 (**AcTre245**) hydrocarbon chains (Fig. 3*A*).

Likewise, MmpL3tb-containing proteoliposomes exhibited no significant H^+ movement when mixed with the buffer at neutral pH. However, the fluorescence of entrapped pyranine either increased or decreased when proteoliposomes were added into the pH 8.0 or the pH 6.0 buffer, respectively (Fig. 2*D*), suggesting that, in the presence of ΔpH, the reconstituted MmpL3tb facilitates a flux of protons across the membrane. This transport of H^+ was modestly stimulated in the presence of the substrate **AcTre67**, as seen from the increased rates of pyranine fluorescence changes (Fig. 2*E*). The rates of fluorescence changes were comparable in the pH 6.0 and pH 8.0 buffers, suggesting a random orientation of the protein in proteoliposomes and that MmpL3tb in both orientations is functional after reconstitution into proteoliposomes. Since **AcTre67** is likely to intercalate only into the outer leaflet phospholipid bilayer of the proteoliposomes and its spontaneous flip-flop is expected to be very slow due to

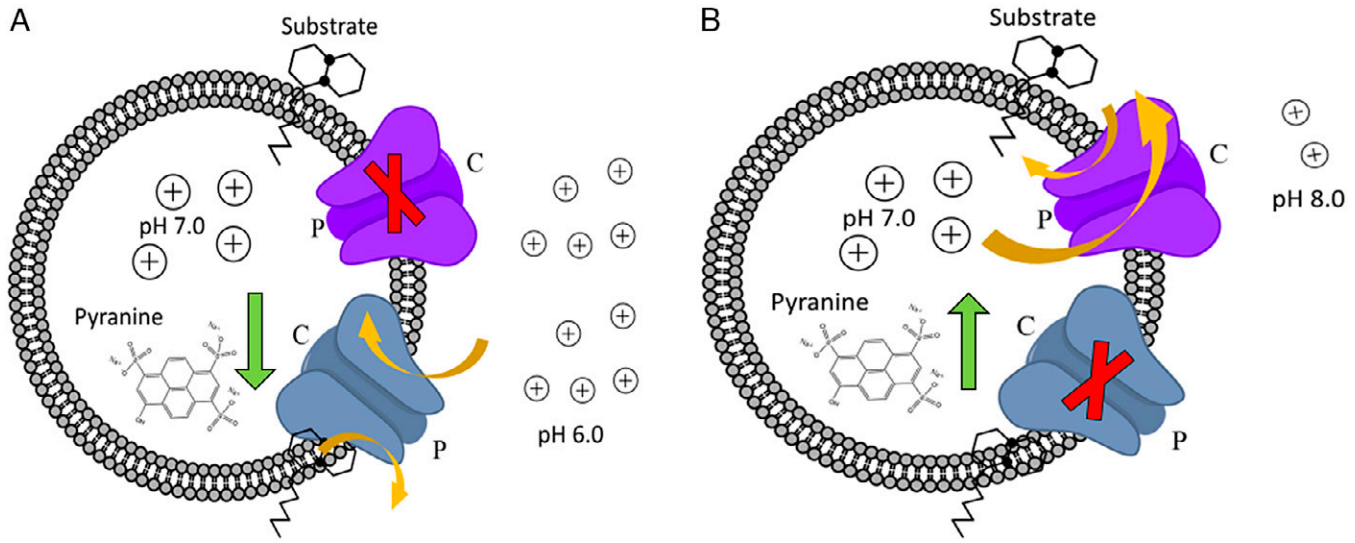

Fig. 1. Schematics of reconstituted proteoliposomes and fluorescence-based proton translocation assays. Transporters are reconstituted into proteoliposomes in both orientations and loaded with the pH-sensitive fluorescent probe pyranine in a buffer of pH 7.0. The proton gradient is established by diluting proteoliposomes either into the buffer of pH 6.0 (*A*) or into the buffer of pH 8.0 (*B*). The fluorescence of pyranine decreases upon protonation in acidic pH and increases upon deprotonation.

the presence of the trehalose headgroup, it is likely that the substrate stimulates the activity of the MmpL3tb vesicles whose substrate binding site is accessible from the outer leaflet of the membrane.

We further tested whether substrate analogs with shorter hydrocarbon tails can also stimulate the proton-translocating activity of the reconstituted MmpL3tb. However, the rate of fluorescence change in the presence of these substrates was even lower than in their absence (Fig. 2*F*), suggesting that the length of the hydrocarbon chain is important for the activity of the MmpL3tb pump. Furthermore, the decreased rates of the MmpL3tb-dependent proton flux suggest that the substrate mimics with short carbon chains might inhibit the activity of the reconstituted MmpL3tb. No effect on the proton-translocating activity of MmpL3tb was found upon addition of trehalose sugar (*SI Appendix*, Fig. S2).

The properties of the reconstituted CmpL1 differed from those of MmpL3tb. We found that CmpL1 proteoliposomes exhibited similar H^+ influx in the pH 6.0 and the pH 7.0 buffers, whereas no significant proton flux could be detected in the pH 8.0 buffer (Fig. 2*G*). Surprisingly, **AcTre67** as well as other analogs did not stimulate the proton flux activity of CmpL1 in either of the tested buffers (Fig. 2*H*). This result suggested that the two transporters differ in the pK_a values of their proton-translocating residues. Alternatively, the reconstituted CmpL1 could be asymmetric such that most of the transporter molecules cannot accept protons from inside of proteoliposomes. To distinguish between these two possibilities, we made MmpL3tb and CmpL1 constructs carrying a TEV cleavage site located between the C termini of the proteins and the affinity purification tags. The expression of MmpL3tb-TEV was too low for biochemical analyses, and we could not assess its orientation in proteoliposomes. However, we were able to purify and reconstitute into proteoliposomes the CmpL1-TEV variant. We found that about half of CmpL1-TEV reconstituted into proteoliposomes was accessible for cleavage by TEV protease (*SI Appendix*, Fig. S3), demonstrating that, in proteoliposomes, CmpL1 adopts a random orientation. Thus, the different properties of CmpL1 and MmpL3tb are likely due to differences in the pK_a values of their proton-translocating residues.

The MmpL3ΔCtb variant reproduced the proton-translocating activity of the whole-length protein (Fig. 2*C* and *SI Appendix*, Fig. S2). This result is consistent with earlier findings that the function of the C-terminal domain is not essential for the transport activities of MmpL3tb. However, biochemical properties of the recombinant MmpL3ΔCtb protein purified from *E. coli* were somewhat different from MmpL3tb, as seen from the lack of stimulation by **AcTre67** at pH 8.0 (Fig. 2*C*). Proteolysis of the TEV site-containing MmpL3ΔCtb-TEV variant confirmed a random orientation of the protein in proteoliposomes but with ~80% preference for the C terminus-out orientation (*SI Appendix*, Fig. S3). Thus, the preferable orientation in proteoliposomes could be the reason for the differences in activities of the reconstituted MmpL3tb and MmpL3ΔCtb transporters.

Thus, both MmpL3tb and CmpL1 reconstituted into proteoliposomes are functionally active and facilitate the flux of protons across the membrane. However, only the activity of the reconstituted MmpL3tb transporter is stimulated by substrate mimics. This stimulation appears to be dependent on the length of the hydrocarbon tails in the substrate mimics.

AcTre67 Substrate Analog Binds MmpL3tb but Not CmpL1. We next used a surface plasmon resonance (SPR) assay to establish whether **AcTre67** substrate mimic binds directly to MmpL3tb and CmpL1. We previously used this approach to analyze the direct interaction of selected inhibitors with purified MmpL3tb (38). For this purpose, the purified CmpL1 and MmpL3tb proteins were immobilized side by side onto the same CM5 Series S sensor chip (GE Healthcare). **AcTre67** and other substrate mimics were injected in increasing concentrations, and binding interactions were analyzed in real time (Fig. 4). Surprisingly, we found that the purified MmpL3tb but not CmpL1 bound **AcTre67**. This result is consistent with the finding that **AcTre67** stimulates the H^+-translocating activity of MmpL3tb but has no effect on CmpL1. Fitting the **AcTre67** sensorgrams into a simple 1:1 binding model yielded the equilibrium dissociation constant K_D of 67 μM, with the relatively fast on-rate but slow off-rate for the **AcTre67**–MmpL3tb interactions (Fig. 4). Thus, the purified MmpL3tb and CmpL1 differ in their interactions with the substrate analog **AcTre67**.

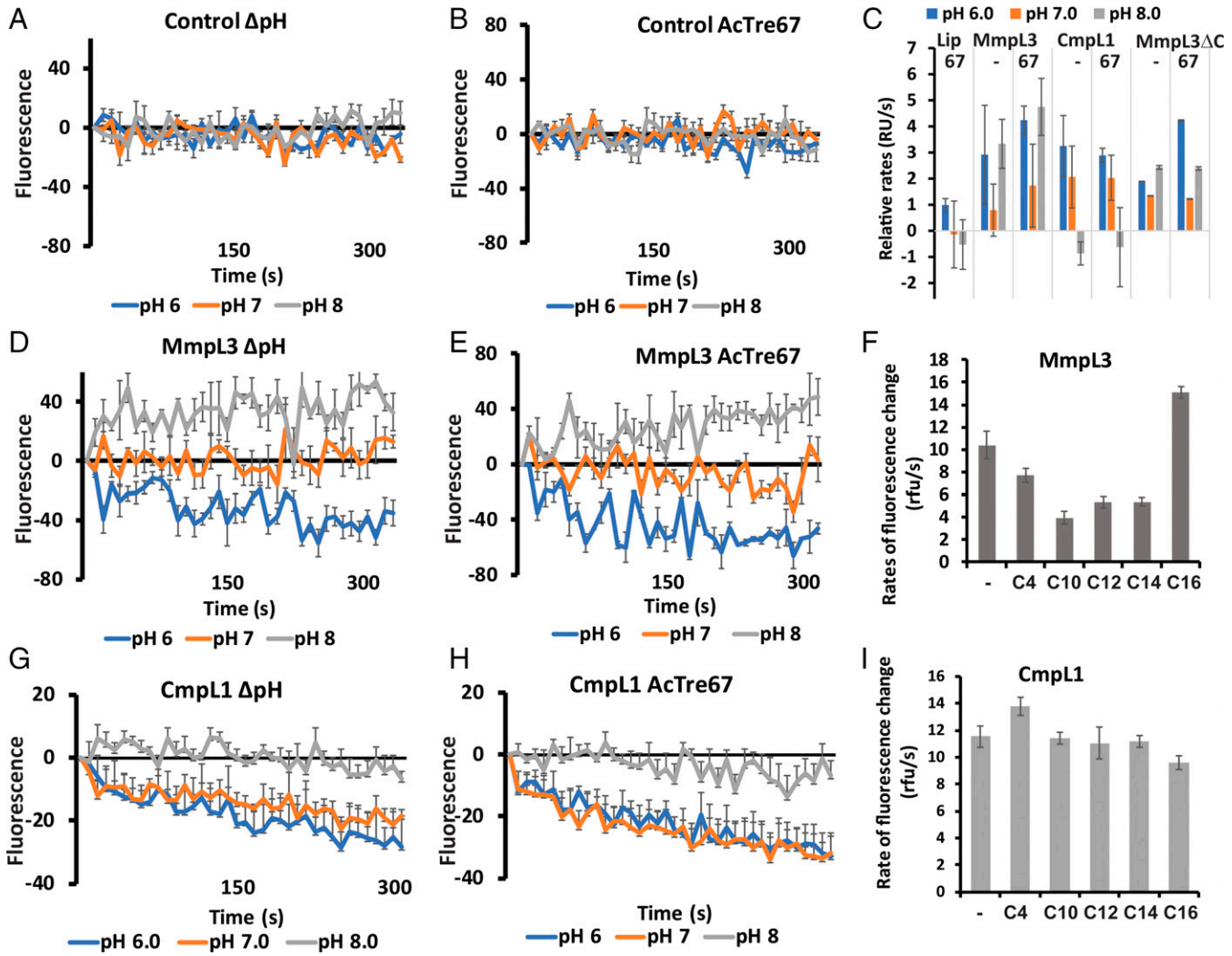

Fig. 2. Proton translocation activities of the purified MmpL3tb and CmpL1 reconstituted into proteoliposomes. Control vesicles (*A* and *B*) and MmpL3tb-containing (*D* and *E*) and CmpL1-containing (*G* and *H*) proteoliposomes were injected into the buffers at different pH values, and fluorescence of entrapped pyranine (λex = 455 nm and λem = 509 nm) was monitored for 5 min at 25 °C. The substrate analog **AcTre67** was added when indicated. Blue lines, pH 6.0 buffer; orange lines, pH 7.0 buffer; gray lines, pH 8.0 buffer. All plots were normalized to zero-time initial fluorescence, and error bars are SD (n = 3). (*C*) Rates of proton transfer (relative fluorescence units per second) in control and MmpL3tb-, CmpL1-, and MmpL3ΔC-containing proteoliposomes were calculated by fitting the individual experimental curves into a simple logarithmic equation and were normalized to the rate of proton leakage in control vesicles; error bars are SD (n = 3). (*F*) The same as in C, but the rates are shown for MmpL3tb proteoliposomes in the pH 6.0 buffer in the presence of indicated substrate analogs. (*I*) The same as in *F* but for CmpL1-containing proteoliposomes.

In agreement with the reconstitution results, which showed no stimulation of H^+-translocating activities of transporters by mimics with shorter hydrocarbon chains (Fig. 2), we found no interactions between these mimics and either protein (*SI Appendix*, Fig. S4). Hence, not only trehalose but also the hydrocarbon tail contributes significantly to substrate binding to MmpL3tb/CmpL1.

Protonation of Glu553 of MmpL3tb Could Promote Diffusion of Substrates into the Periplasmic Binding Site. Previous studies showed that the truncated MmpL3ΔCtb variant is a monomer (27–29). Chemical cross-linking experiments showed that the purified whole-length MmpL3tb, but not MmpL3ΔCtb, can be cross-linked into higher-molecular-weight complexes, possibly a trimer (Fig. 5 *A* and *B*). This result provides further biochemical evidence in support of oligomerization of MmpL3tb and its homologs (20, 25, 26, 41). To resolve possible structural differences in MmpL3tb at different pH values, we built structural models of an MmpL3 trimer (Fig. 5 *C* and *D*) and a monomer (*SI Appendix*, Fig. S5) from *M. smegmatis* (MmpL3smg). We used the existing structure of the C-terminal truncated MmpL3smg monomer (Protein Data Bank [PDB] ID: 6AJF) (27), a close homolog of MmpL3tb (see *Materials and Methods* for details). The complementation studies demonstrated that these two proteins are functionally equivalent (23). We then created six distinct models (three for the trimer and three for the monomer) corresponding to the states at pH 6.0, 7.0, and 8.0, by protonating or deprotonating specific residues according to their pK_a values (*SI Appendix*, Table S1). All these residues are conserved between the two MmpL3 homologs, except His540 in MmpL3smg, which is replaced by Lys535 in MmpL3tb. The analyzed aspartate and glutamate residues, but not the histidine residues, are also conserved in CmpL1 (*SI Appendix*, Fig. S6). The MmpL3smg residues Asp256 and Asp645 located in the transmembrane α-helices TM4 and TM10, respectively, and the analogous residues in MmpL3tb and CmpL1 are functionally essential and thought to be critical to the proton transfer activity of these transporters (20). The models were simulated for 100 ns each in an *E. coli* lipid membrane, matching the experimental setup.

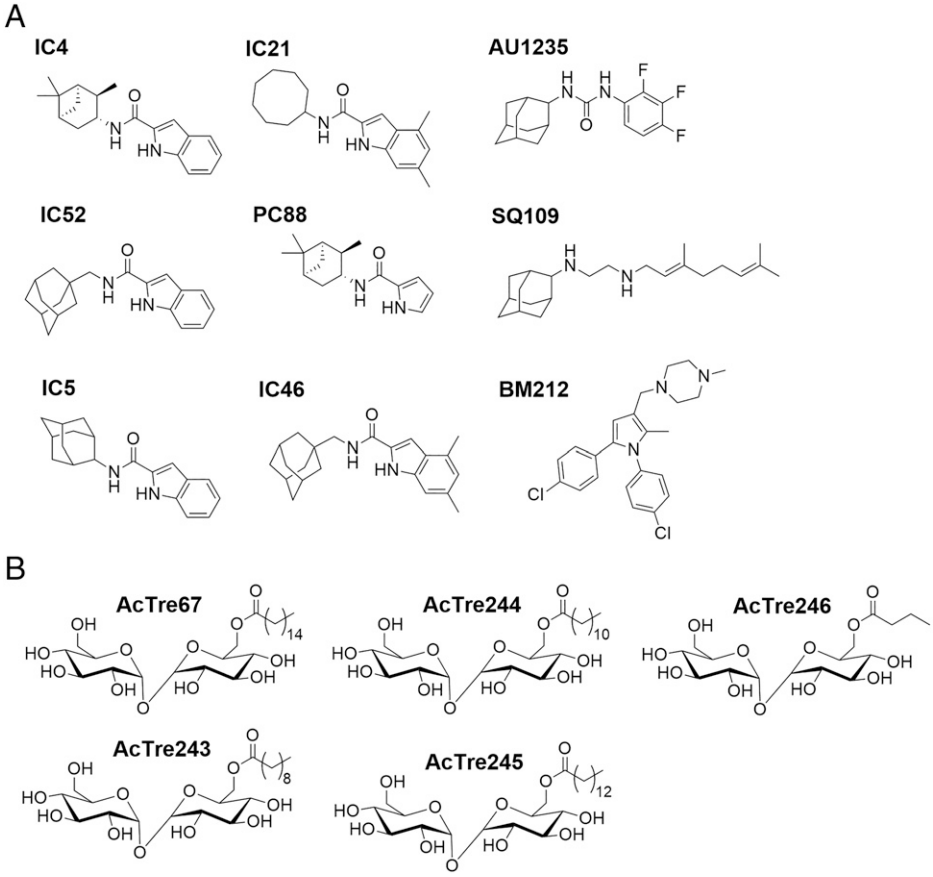

Fig. 3. Substrate analogs (*A*) and inhibitors (*B*) of MmpL3tb and CmpL1 transporters.

No significant changes were found in the transmembrane domains of the models, in part because the functionally essential Asp256 and Asp645 are predicted to be protonated irrespective of the pH in the range 6.0 to 8.0 (*SI Appendix*, Table S1). However, aligning to the trimer showed that the pH 6.0 model was slightly more dynamic than the pH 7.0 and pH 8.0 models, according to their root-mean-square deviation (*SI Appendix*, Fig. S7). Upon closer examination of the trajectories, we found that the movement involves the periplasmic loop containing Arg523, which corresponds to Pro518 in MmpL3tb (*SI Appendix*, Fig. S8). In the MmpL3smg trimer models at pH 7.0 and pH 8.0, this residue makes a hydrogen bond with the conserved Glu553 in the periplasmic extension of TM8 for 50 to 100% of the 100-ns simulations, depending on the protomer. We did not see the same interactions in the monomer models (*SI Appendix*, Fig. S5). In the pH 6.0 trimer model, Glu553 is protonated and, thus, does not interact with Arg523, instead freeing the loop to move away from the protein (Fig. 5*E*). In the crystal structure of MmpL3smg, this loop separates the two putative substrate binding sites, one located at the protein interface with the outer leaflet of the inner membrane (interfacial) and another located between the periplasmic PN and PC domains of MmpL3smg (periplasmic) (27). In the crystal structures, these sites are occupied by either phosphatidylethanolamine (PE) (27) or by the substrate mimic detergent 6-n-dodecyl-α, α-trehalose (6DDTre) (28), suggesting that the Glu553 loop may be involved in the substrate transfer between the two binding sites. The importance of this loop is further validated by our previous finding that substitutions of Gly543 (Gly548 in MmpL3smg) and Asp550 (Asp555 in MmpL3smg) significantly hinder the growth of *Mtb* (20).

Intriguingly, in all simulations (monomer and trimer) and for all protomers, one to two PE molecules spontaneously diffused out of the outer leaflet of the membrane and into the interfacial binding site embraced by TM7 through TM10 of MmpL3smg (Fig. 5 *F* and *G*), perfectly matching the PE binding site observed in the crystal structure (PDB ID: 6OR2) (27). Thus, in the reconstituted proteoliposomes, this interfacial substrate binding site of MmpL3 is likely occupied by phospholipids. We next replaced the PE molecule(s) in this site on each protomer for the pH 7.0 model with the substrate analogs **AcTre67**, **AcTre243**, **AcTre244**, **AcTre245**, and **AcTre246** (Fig. 3*A*) and simulated each of the five systems for an additional 100 ns. We tracked the positions of the substrate analogs over time (*SI Appendix*, Fig. S9). While we did not observe a translocation of the substrate analogs into the periplasmic binding site during the 100-ns simulations, two copies of the analog with the shortest carbon tail, **AcTre246** (C4), dissociated from the site and left the membrane entirely. We also tracked the fraction of surface area of the substrate in contact with the protein (*SI Appendix*, Fig. S10). Each substrate had 20 to 70% of its surface area ensconced by the protein. One copy of **AcTre244** briefly dissociated from the protein but quickly returned. Trehalose sugars placed into the binding site left it almost immediately even if the binding of trehalose was stabilized by extra bonds based on the crystal structure (*SI Appendix*, Fig. S10*F*).

Thus, the inability of the shorter hydrocarbon chains to stimulate the proton-translocating activity of MmpL3 (Fig. 2) and to bind to the protein in SPR assays (*SI Appendix*, Fig. S4) could be explained by their lower affinities to the interfacial binding site and dissociation from the lipid bilayer, which

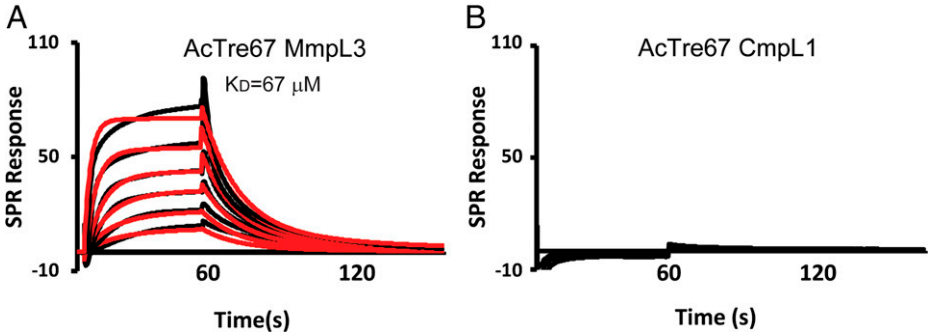

Fig. 4. Kinetics of **AcTre67** interactions with the purified MmpL3tb and CmpL1 proteins. MmpL3tb (*A*) and CmpL1 (*B*) were immobilized at densities of 12,450 and 17,025 response units (RU), respectively. Compounds were injected at a 20 μL/min flowrate in the running buffer containing 25 mM Hepes-KOH (pH 7.4), 150 mM NaCl, 0.2% Triton X-100, 5% dimethyl sulfoxide. Sensorgrams (black lines) of twofold dilutions from 400 μM to 12.5 μM of **AcTre67** are fit globally (red lines) into a 1:1 binding model.

further reduces effective concentrations of these substrate mimics. The lack of binding and stimulation of CmpL1 activity by **AcTre67** further suggests that the interfacial site of CmpL1 differs from that of MmpL3. Indeed, the analogous region of CmpL1 protein is 12 residues shorter than in its MmpL3 homologs, and the amino acid residues of MmpL3smg Lys528, Asp531, and His558 that interact with a PE molecule in the interfacial site (Fig. 5*G*) are conserved in MmpL3tb but not in CmpL1 (*SI Appendix*, Fig. S8).

Inhibitors of MmpL3 Comprise Compounds with both Narrow and Broad Target Specificities. To identify inhibitors that are specific to MmpL3tb and/or *C. glutamicum* CmpL1, we first analyzed their antibacterial activities. Previous studies showed that, in *C. glutamicum,* two of the four CmpL proteins, CmpL1 and CmpL4, are functionally redundant in the export of TMCM, and that only the double-knockout mutant in both genes encoding these proteins is nonviable (19, 21). To identify inhibitors with both narrow and broad specificity, we used *C. glutamicum* strains producing either CmpL1 or CmpL4 transporter and a panel of structurally diverse inhibitors of MmpL3tb.

We focused on six previously reported representative MmpL3tb inhibitors: the adamantyl urea **AU1235** (23), the 1,2-diamine **SQ109** (42), the tetrahydropyrazolopyrimidine **THPP1** (43), the 1,5-diarylpyrrole **BM212** (44), and the indole-2-carboxamides (IC) **NITD-304** and **NITD-349** (45)

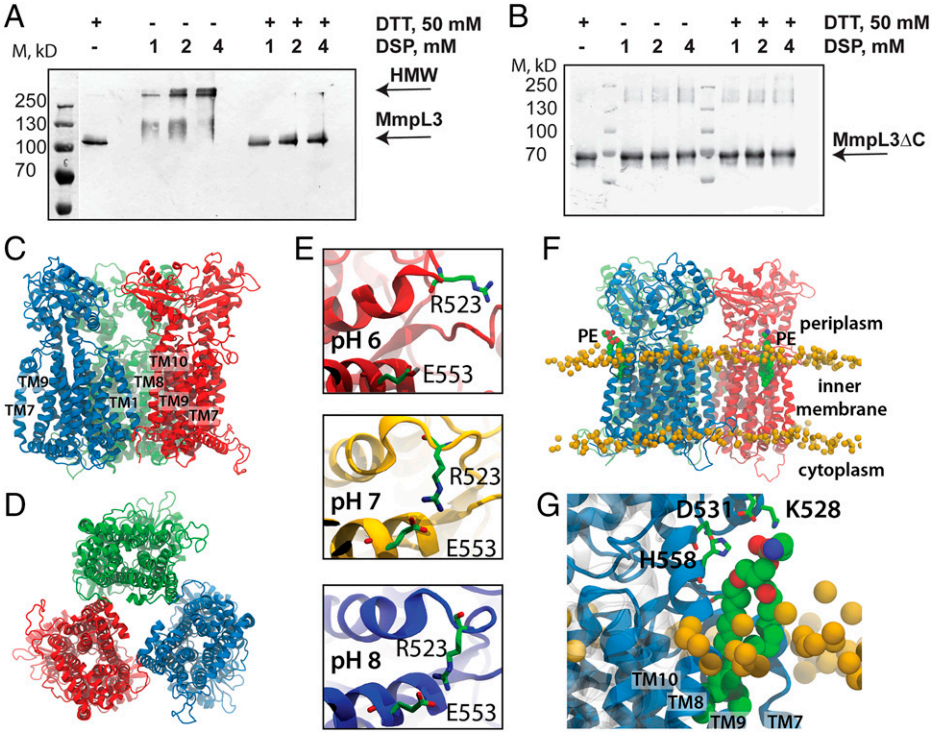

Fig. 5. Oligomerization and simulations of MmpL3. (*A*) Purified MmpL3tb was treated with increasing concentrations (millimolars) of a primary amine-reactive, thiol-cleavable cross-linker, dithiobis(succinimidyl propionate (DSP). After 45-min incubation at room temperature, cross-links were reversed by incubation with 50 mM dithiothreitol (DTT) for 30 min at 37 °C. Samples were resolved by 8% sodium dodecyl sulfate polyacrylamide gel electrophoresis, and MmpL3-containing bands were visualized by immunoblotting with an anti-His monoclonal antibody (Sigma). The positions of the monomeric MmpL3 and its cross-linked high molecular weight (HMW) species are indicated by arrows. (*B*) The purified MmpL3ΔCtb was processed and analyzed as described in *A*. Unidentified smearing bands cross-reacting with an anti-His monoclonal antibody could be seen between the 130- and 250-kDa markers. The amounts of these bands were unaffected by chemical cross-linking and DTT. (*C* and *D*) Modeled trimer, colored blue, red, and green, of MmpL3smg viewed from the membrane plane (*C*) and from the periplasmic side (*D*). (*E*) Interaction between Arg523 and Glu553 at pHs 6, 7, and 8. Note that, at pH 6, Glu553 is protonated. (*F*) MmpL3smg trimer in a membrane after 100-ns simulation at pH 7. The orange spheres represent phosphorus atoms defining the membrane planes. Two lipids bound that are bound to the periplasmic-leaflet binding site are highlighted as spheres colored by atom type (green, carbon; red, oxygen; blue, nitrogen). (*G*) Close-up of one bound lipid interacting with His558, Asp531, and Lys528.

(Fig. 3*B*). In addition, we generated a series of 68 novel IC and analogs, including pyrrole-2-carboxamides (PC), imidazole-2-carboxamides (ImC), and α-hydroxyphenyl-2-carboxamides (αHC) as well as nine quinazolines (QZ). IC and QZ analogs were synthesized according to our previous reports (30, 46). ICs were designed to optimize high antitubercular potency based on previously published structure-activity-relationship (SAR) (30, 34, 45, 47–51). PC, ImC, and αHC miniseries were designed to explore structural determinants of the IC scaffold. Lastly, QZs were tested as a structurally unique class of ICs to further determine the promiscuity of MmpL3tb.

Minimum inhibitory concentrations (MIC) of the inhibitors were measured using serial twofold broth dilutions for *Mtb* H37Rv mc^{2}6206, *C. glutamicum* ATCC 13032, and triple-knockout *C. glutamicum* mutants LY108 (Δ*cmpL1* Δ*cmpL2* Δ*cmpL3*) and LY109 (Δ*cmpL2* Δ*cmpL3* Δ*cmpL4*) producing only CmpL4 or CmpL1, respectively (Table 1). **SQ109** and **BM212** compounds inhibited the growth of all tested strains, providing further evidence for their broad spectrum of activity (38). In contrast, the tetrahydropyrazolo[1,5-a]pyrimidine-3-carboxamide **THPP1**, as well as most of the compounds from the IC series including **NITD-304** and **NITD-349**, inhibited growth of *Mtb* at low micromolar concentrations but had no activity against the *C. glutamicum* strains (MIC values over 500 μM). However, IC derivatives, **IC4**, **IC21,** and **IC52,** and a PC, **PC88** (Fig. 3*B*), also inhibited the growth of *C. glutamicum* at low and mid micromolar concentrations. Their antibacterial activities were specific to CmpL1, as they inhibited the growth of LY109 (CmpL1 dependent) strain but not LY108 (CmpL4 dependent). Thus, in addition to MmpL3tb, these compounds specifically target CmpL1, albeit with different efficiencies. Both **IC4** and **IC21** have nanomolar MIC values against *Mtb* H37Rv mc^{2}6206 and are the best inhibitors of *C. glutamicum* LY109, with MIC values of 4 and 32 μM, respectively (Table 1). **IC52** and **PC88** are active against both MmpL3tb and CmpL1 transporters at micromolar concentrations.

Taken together, these results show that the inhibitors vary in their target specificities, with most of the inhibitors effective possibly only against MmpL3tb. **SQ109** and **BM212** have broad specificity and, in addition to MmpL3tb, seem to act against both CmpL4 and CmpL1. Both **BM212** and **SQ109** are known to have off-target effects on the membrane potential (52–55). However, the primary bactericidal activity of **BM212** is likely to be due to MmpL3tb and CmpL1 inhibition, because spontaneous resistant mutants with single nucleotide substitutions in *mmpL3* are easily isolated, and this inhibitor affects the proton motive force (PMF) only at relatively high concentrations (above MIC) (44, 52). On the other hand, it is almost impossible to isolate spontaneous resistant mutants against **SQ109**, which is likely to primarily act by dissipating the PMF (42). A few inhibitors appear to be active against CmpL1 and MmpL3tb. Since CmpL1 and CmpL4 are interchangeable in their physiological functions, these results further suggest that the mechanism of action of these inhibitors is sensitive to the structural features of the transporters.

Inhibitors Interact Directly with MmpL3tb and CmpL1. Inhibitors acting specifically on MmpL3tb and CmpL1 are expected to directly bind to the target proteins. We again used an SPR assay to compare the binding mechanisms and affinities of inhibitors displaying broad or narrow target specificities. In agreement with previous studies (38), **AU1235**, **SQ109**, and **BM212** inhibitors all bound MmpL3tb with micromolar affinities (Fig. 6 and *SI Appendix*, Table S2). Interestingly, these inhibitors bound to CmpL1 with nearly identical binding

Table 1. MICs (micromolar) of tested compounds

Compound	*Mtb* H37Rv mc^{2}6206	*C. glutamicum* ATCC 13032	*C. glutamicum* LY108 (CmpL4)	*C. glutamicum* LY109 (CmpL1)
IC2	1.02	>500	>500	>500
IC4	0.05	>500	>500	4
IC5	1.32	>500	>500	>500
IC10	>38.7	>500	>500	>500
IC12	19.50	>500	>500	>500
IC21	0.07	>500	>500	31.2
IC 41	1.09	>500	>500	>500
IC 42	>17.45	>500	>500	>500
IC43	>15.98	>500	>500	>500
IC46	0.48	>500	>500	>500
IC 50	0.12	>500	>500	>500
IC52	25.9	>500	>500	31.2
IC65	6.17	>500	>500	>500
QZ76	>104.18	>500	>500	>500
PC88	8.12	>500	>500	65.2
IC90	54.02	>500	>500	>500
PC91	32.50	250	250	250
IC92	12.34	>500	>500	>500
αHC9595	112.21	>500	>500	>500
PC96	155.23	>500	>500	>500
SQ109	1.82	125	62.5	62.5
BM212	19.36	30	30	30
NITD304	0.01	>500	>500	>500
NITD349	0.03	>500	>500	>500
THPP-1	5.38	>500	>500	>500
AU1235	1.2	>500	>500	>500

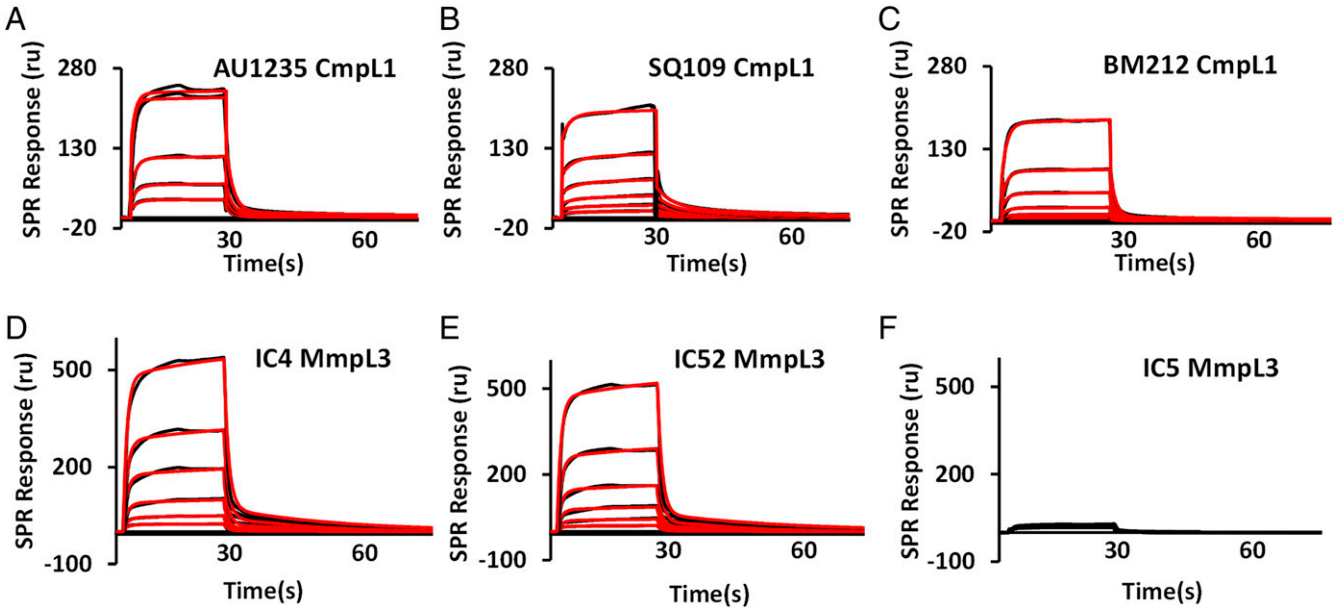

Fig. 6. Kinetics of interactions of the indicated inhibitors with the purified CmpL1 (*A*–*C*) and MmpL3tb (*D*–*F*). Conditions are the same as in Fig. 3. Compounds **AU1235** (*A*), **SQ109** (*B*), **IC4** (*D*), **IC52** (*E*), and **IC5** (*F*) were injected at twofold increasing concentrations from 12.5 μM to 400 μM. **BM212** (*C*) was injected at twofold increasing concentrations from 1.86 μM to 60 μM. Sensorgrams (black lines) are fit globally (red lines) into a 1:1 binding model. Rates, affinities, and residuals for the fitted data are shown in *SI Appendix*, Table S2.

mechanisms and affinities (Fig. 6), providing further support for the broad target specificities of these compounds.

We next analyzed the binding activities of **IC4**, **IC21**, and **IC52** that, in addition to inhibiting *Mtb* growth, had the lowest MIC values against *C. glutamicum* LY109 (Table 1). For both CmpL1 and MmpL3tb, we again found nearly identical binding mechanisms for these compounds (Fig. 6). In contrast, **IC5**, a structural analog of **IC52**, which is active against MmpL3tb but shows no inhibitory activity against any *C. glutamicum* strain, exhibits a remarkably different binding mechanism (Fig. 6). Removal of the methylene group linking the adamantyl group and amide nitrogen resulting in **IC5** almost completely abolished binding interactions with MmpL3tb and CmpL1. Thus, there is no straightforward relationship between the binding kinetics of inhibitors to MmpL3tb and CmpL1 and their growth inhibition activities in vivo.

Proton-Translocating Activities of MmpL3tb and CmpL1 Transporters Are Susceptible to Chemical Inhibition. Next, we sought to test whether the inhibitors with the antibacterial activities against both corynebacteria and mycobacteria would also inhibit the biochemical activities of the reconstituted CmpL1 and MmpL3tb transporters. In this assay, we preincubated MmpL3tb- and CmpL1-containing proteoliposomes and empty control vesicles equilibrated in the pH 7.0 buffer with the substrate **AcTre67** and then mixed them into the buffers containing increasing concentrations of an inhibitor. The change in pyranine fluorescence and, hence, proton flux was measured as described in Fig. 1. The control empty vesicles preincubated with **AcTre67** and then exposed to the inhibitors **IC21**, **IC52**, and **IC4** showed no significant proton flux under the testing conditions, suggesting that neither the substrate nor the inhibitors affected the integrity of the phospholipid bilayer of the vesicles (Fig. 7 *A*–*C*).

In contrast, the proton-translocating activity of MmpL3tb was inhibited by all three inhibitors, albeit in a pH-dependent manner (Fig. 7 *A*–*C*). In the pH 6.0 buffer, **IC4** and **IC21** inhibited the proton-translocating activity of MmpL3tb in a concentration-dependent manner. The inhibitory effect of **IC52** was the same at the three tested concentrations, reducing the rate of proton flux by threefold. This result suggests that not all MmpL3 molecules are inhibited by **IC52** under these conditions. In contrast, only **IC52** exhibited an inhibitory activity when the assays were carried out in the pH 8.0 buffer, whereas neither **IC21** nor **IC4** inhibited the reconstituted MmpL3 at this pH (Fig. 7*D*). Furthermore, **IC21** appears to stimulate the proton efflux from the proteoliposomes. This result suggests that either the activity of inhibitors is sensitive to pH due to the presence of ionizable groups or that the inhibitors have an affinity for a specific orientation of MmpL3tb–**AcTre67** complex in the proteoliposomes.

Although the activity of the reconstituted CmpL1 was not stimulated by substrate mimics, the spontaneous H^+ flux was still observed in these proteoliposomes, but only in the pH 6.0 buffer (Fig. 2*H*). This **AcTre67**-independent activity was also sensitive to the presence of inhibitors (Fig. 7 *A*–*C*). The CmpL1-dependent proton flux was reduced when increasing concentrations of any one of **IC21**, **IC52**, and **IC4** were added to the reaction. Surprisingly, in the pH 8.0 buffer, **IC52** and **IC4** stimulated the CmpL1-dependent efflux of H+ from the proteoliposomes (Fig. 7*E*).

Thus, IC inhibitors interact with MmpL3tb and CmpL1 and modulate their proton-translocating activities.

Discussion

MmpL3/CmpL1 and their analogs are the focus of intense investigations due to the importance of these proteins in the physiology of CMN species and antituberculosis drug discovery (37, 38, 56). Despite advances in the structural and functional study of these proteins, their biochemical characterization is lagging, largely because of difficulties with analyses of membrane proteins, and the complexities of their physiological substrates. In this study, we successfully purified, from native membranes, the whole-length MmpL3tb and *C. glutamicum* CmpL1 proteins and reconstituted them into proteoliposomes.

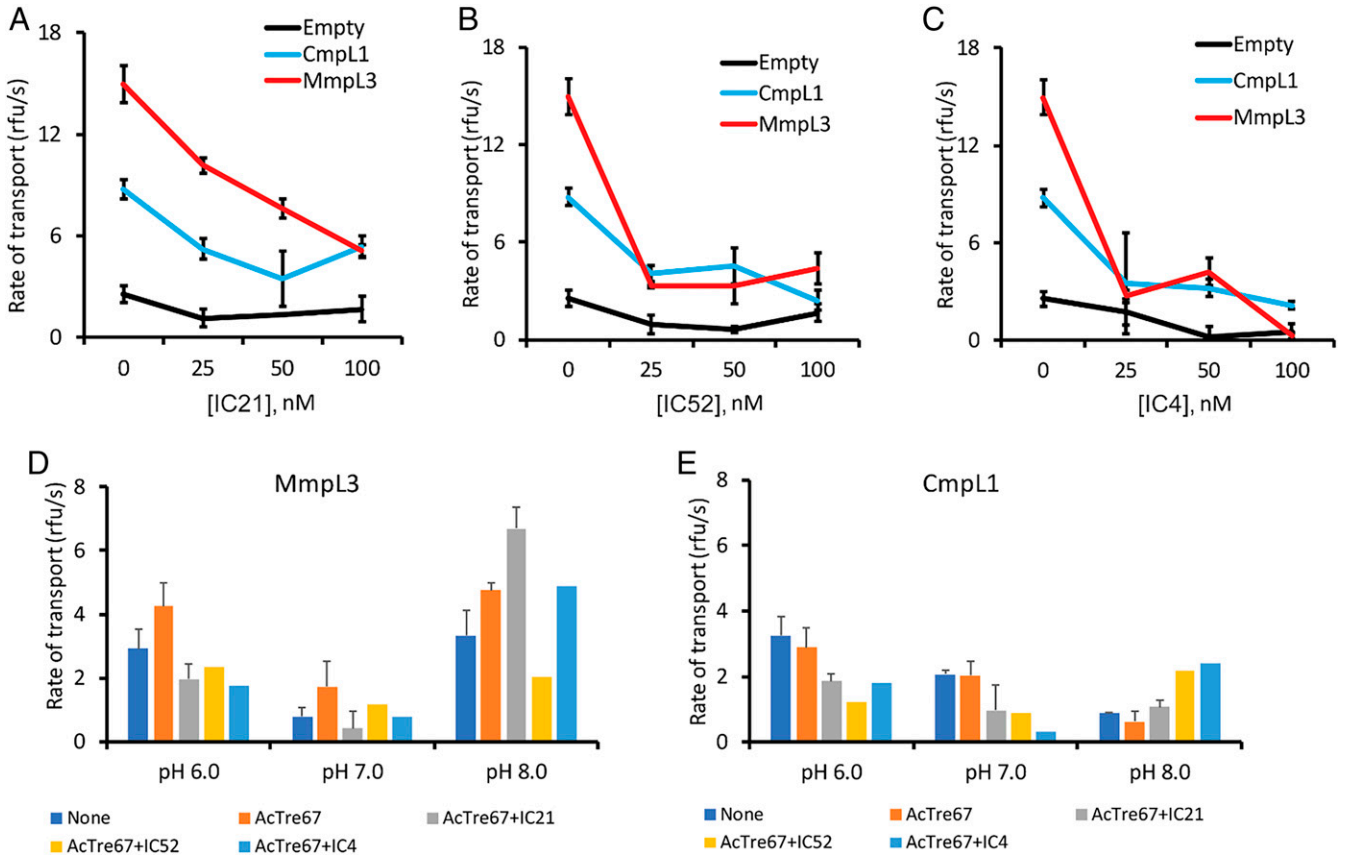

Fig. 7. Inhibition of proton-translocating activities of MmpL3tb and CmpL1 reconstituted into proteoliposomes. (*A*) Control empty vesicles (black line), CmpL1 proteoliposomes (blue line), and MmpL3tb proteoliposomes (red line) were incubated with **AcTre67** for 5 min and then added to the pH 6.0 buffer containing **IC21** at twofold increasing concentrations. Fluorescence of entrapped pyranine was monitored for 5 min at 25 °C. Rates of transport were calculated and plotted as a function of inhibitor concentration. Error bars are SD (n = 3). (*B*) The same as in *A*, but buffer was supplemented with **IC52**. (*C*) The same as in *A*, but buffer was supplemented with **IC4**. (*D*) Empty vesicles and MmpL3tb proteoliposomes in the pH 7.0 buffer were preincubated with 50 nM **AcTre67** for 5 min and then added to the indicated pH buffer containing a 50-nM inhibitor. Rates of proton transport in proteoliposomes were normalized to the rate in empty vesicles. Error bars are SD (n = 3). (*E*) The same as in *D* but for CmpL1 proteoliposomes.

Our studies have demonstrated that both proteins facilitate proton translocation across a phospholipid bilayer and that this activity can be modulated by substrate analogs IC inhibitors. The C-terminal cytoplasmic domain of MmpL3tb is not required for these activities (*SI Appendix*, Fig. S2) but contributes to protein oligomerization (Fig. 5 *A* and *B*) and subcellular localization (20, 26).

The proton translocation domains of RND transporters are highly conserved and likely to use the same molecular mechanism (28). Two highly conserved pairs of Asp256—Tyr646 and Tyr257—Asp645 residues linking TM4 and TM10 of MmpL3smg by hydrogen bonds and the analogous pairs in MmpL3tb and CmpL1 are likely to be involved in the translocation of protons. Although both reconstituted MmpL3tb and CmpL1 facilitate proton translocation across phospholipid bilayers of proteoliposomes (Fig. 3), it remains unclear whether these transporters are fully reversible and can move substrates in both directions across the membranes depending on the directionality of the pH gradient. RND transporters of gram-negative bacteria such as AcrB or MexB are thought to be unidirectional because, during the transport process, their substrate binding sites face only one side of the membrane, the periplasmic side (57–59). Similarly, the recently reported structures of the C-terminal truncated MmpL3smg and MmpL3tb suggested the substrate binding site to be in the periplasmic domain of the protein, and away from the proton translocation transmembrane path (27–29). In contrast, analyses of protein activities in bacterial membrane vesicles suggested a flippase-like mechanism that implies interactions of transporter with its substrate on both sides of the membrane (24). During reconstitution into proteoliposomes, insertion of proteins into phospholipid bilayers is a spontaneous process resulting in two opposite orientations of proteins in the membrane: The periplasmic domains of MmpL3tb/CmpL1 face either the external buffer or the internal lumen of the lipid vesicles (Fig. 1 and *SI Appendix*, Fig. S3). Bidirectional proton fluxes in MmpL3tb proteoliposomes (Fig. 2) and the site-directed cleavage of MmpL3tbΔC and CmpL1 by TEV protease (*SI Appendix*, Fig. S3) suggested that all three proteins are reconstituted into proteoliposomes in both orientations. However, CmpL1-containing proteoliposomes were not capable of proton efflux in the pH 8.0 buffer, suggesting the lack of activity from the inside-out proteins. Interestingly, the two proteins differ dramatically in their pI values, with MmpL3tb carrying an overall positive (pI = 9.48) and CmpL1 carrying an overall negative (pI = 4.70) charge at the physiological pH. These differences in the composition of chargeable amino acid residues could contribute to the apparent single-sided activity of the reconstituted CmpL1.

The two proteins further differed in their response to the substrate mimic **AcTre67**. After incubation with this substrate, we discovered a moderate but reproducible stimulation of flux of protons mediated by MmpL3tb and MmpL3ΔCtb in either of the two directions. In contrast, no stimulation of proton movement due to **AcTre67** was observed in CmpL1. This

result suggested that **AcTre67** binds to MmpL3tb in either of the two orientations, whereas CmpL1 appears to not recognize it as a substrate. The lack of interaction of **AcTre67** with CmpL1 was further confirmed in the SPR experiments (Fig. 4). The interfacial binding site is likely to be first to accommodate the substrate for removal from the membrane. In the MmpL3smg model, this site is capped by a loop stabilized by the hydrogen bond between Arg523 and Glu553 (Fig. 5). In the pH 6.0 model, Glu553 is protonated, opening the loop for possible further transfer of the substrate into the periplasmic site and away from the membrane. Although the Arg523 of MmpL3smg is replaced with a proline residue in MmpL3tb (*SI Appendix*, Fig. S8), there are several positively charged residues in proximity that could bind with Glu548 of MmpL3tb (equivalent to Glu553 in MmpL3smg).

Unlike TMMs, **AcTre67** does not carry a mycolic acid chain and neither does it carry an acetylated mycolic acid chain apparently required for in vivo transport recognition (18). These differences could be responsible for the modest effects of **AcTre67** on the proton-translocating activity of MmpL3tb. Alternatively, a copurifying substrate or a phospholipid occupying the substrate binding site of CmpL1 and/or MmpL3tb, as was found in the crystal structure of MmpL3smg (27, 28), could affect the activities of the reconstituted transporters. The molecular dynamics (MD) simulations showed that PE phospholipids dissociate from the membrane bilayer to bind to the interfacial binding site of MmpL3smg (Fig. 5 and *SI Appendix*, Fig. S5). This result further suggests that the affinities of lipids and substrates to this site are higher than their affinities to the bilayer.

Nevertheless, **AcTre67** appears to be a preferable substrate of MmpL3tb, because mimics with shorter hydrocarbon tails failed to bind the protein and to stimulate proton flux. The mycobacterial mycolic acid species are generally longer in both the α-branch and merochain as compared to the shorter corynemycolates found in corynebacterial species (8). It is possible that the fatty acid tail contributes to the affinity to the interfacial binding site and to coupling of substrate binding and proton translocation. As seen in the MD simulations (*SI Appendix*, Fig. S9), trehalose and the substrate mimic with the shortest hydrocarbon tail dissociate from the interfacial site and leave the bilayer. Such behavior would significantly reduce the effective concentration of substrates available to the reconstituted transporter. The binding site of CmpL1 is apparently smaller and different, as seen from the alignment of the protein sequences (*SI Appendix*, Fig. S8).

The effects of inhibitors were dependent, again, on both the pH gradient direction and the protein. Although the proton-translocating activities of both proteins in the pH 6.0 buffer were impaired in the presence of **IC21**, **IC52**, and **IC4**, the effect in the pH 8.0 buffer was both protein and inhibitor dependent. **IC52** inhibits MmpL3-dependent proton fluxes in either of the two protein orientations, whereas **IC4** and **IC21** inhibit the right-side-out but stimulate inside-out orientation of the protein. This result suggests that **IC52** can access its binding site more readily from either the cytoplasmic or periplasmic side of the protein, while there is a preferred MmpL3 conformation and orientation for binding access for both **IC4** and **IC21**. Our results suggest that, depending on how these inhibitors interact with the transporter, they can either inhibit its transport activity or cause leakage of protons, potentially dissipating the proton gradient across the cytoplasmic membrane.

Finally, these novel IC compounds designed as MmpL3tb inhibitors and possessing potent antitubercular properties were shown to have antibacterial activities against a *C. glutamicum* strain in which CmpL1 is essential for viability. We were able to demonstrate, via SPR interaction, the effects of minor changes to chemical scaffolds that impede the interaction of compounds with the targets and further suggest a discrete structural vulnerability in the homologous transporters.

Materials and Methods

Strains and Growth Conditions. *M. tuberculosis* H37Rv mc^2 6206 (Δ*panCD* Δ*leuCD*) was grown at 37 °C in Middlebrook 7H9-OADC (oleic acid, bovine albumin, sodium chloride, dextrose, and catalase), 0.05% tyloxapol supplemented with 0.2% casamino acids, 48 μg/mL pantothenate, and 50 μg/mL L-leucine. *M. smegmatis* mc^2 155 was grown at 32 °C in Middlebrook 7H9 broth+10% ADC supplement with 0.05% Tween 80 with shaking. For *C. glutamicum* strains, American Type Culture Collection (ATCC) 13032 strain (wild type) and its derivatives LY108 (Δ*cmpL1* Δ*cmpL2* Δ*cmpL3*), and LY109 (Δ*cmpL2* Δ*cmpL3* Δ*cmpL4*) (19) were grown at 30 °C in 2xTY media with shaking. For *M. smegmatis*, hygromycin B (50 μg/mL) and kanamycin (25 μg/mL) were used as selection markers, and, for *C. glutamicum*, kanamycin (25 μg/mL) was used as a selection marker. *E. coli* Rosetta(DE3) was grown in Luria-Bertani broth at 37 °C with shaking.

Construction of Plasmids. To construct pET:*mmpL3ΔCtb*, the DNA fragment encoding amino acid residues 1 to 767 was amplified by PCR and cloned into NcoI and XhoI sites of pET21a(+) vector. To insert TEV cleavage sites, synthetic DNA fragments spanning partial Rv0206 (*mmpL3*) and Ncgl2769 (*cmpL1*) sequences, followed with the TEV site and His-tag, were synthesized by Integrated DNA Technologies. The fragments were digested with restriction enzymes and cloned into the matching sites of *pMVGH1-mmpL3tb,* pML1, and pET:*mmpL3ΔCtb* to generate fusions with the TEV site and affinity tags. All constructs were verified by DNA sequencing.

Protein Purification. MmpL3tb was purified as described before (38), with the following modifications. Briefly, cell pellet from 1 L of culture of *M. smegmatis ΔmmpL3* cells harboring pMVGH1:*mmpL3tb* membrane pellets were solubilized for 4 h to 12 h at 4 °C in TS Buffer (20 mM Tris·HCl [pH 8.0], 150 mM NaCl, 2% Triton X-100). Insoluble material was removed via ultracentrifugation at 185,000 × *g*, at 4 °C for 1 h, supernatant was collected, and NaCl concentration was increased to 200 mM (final). The sample was then passed through a HiTrap Q-FF (5mL; GE Healthcare) anion exchange column at a flow rate of 0.5 mL/min. Flow-through was collected and adjusted to 400 mM NaCl and 10 mM imidazole (final concentrations) and loaded onto His-Bind affinity resin (Novagen). The column was washed two times with 10 column volumes of TW Buffer (20 mM Tris·HCl [pH 8.0], 400 mM NaCl, 20 mM imidazole, 0.2% Triton X-100), and then the column was washed two times with 10 column volumes of HW Buffer (20 mM Hepes-KOH [pH 8.0], 400 mM NaCl, 20 mM imidazole, 0.2% Triton X-100). MmpL3 was then eluted six times with 0.5CV of HE Buffer (20 mM Hepes-KOH [pH 8.0], 400 mM NaCl, 500 mM imidazole, 0.2% Triton X-100).

C. glutamicum CmpL1 and CmpL1-TEV were purified as described previously (19), with the exception that n-dodecyl β-D-maltoside (DDM) was omitted for Triton X-100 in solubilization buffer (2% Triton X-100) and washing and elution buffers (0.2% Triton X-100).

MmpL3ΔCtb and MmpL3ΔCtb-TEV were purified from *E. coli* Rosetta (DE3) cells as described previously (27), with the following modifications. MmpL3ΔCtb was solubilized from total membrane fractions in HS buffer (50 mM Hepes [pH 7.0], 150 mM NaCl, 2% Triton X-100, 1 mM phenylmethylsulfonyl fluoride) at 4 °C overnight. The extracted sample was then loaded onto His-Bind affinity resin (Novagen), and MmpL3ΔCtb was purified as described above for the whole-length MmpL3.

MIC Assays. Minimal inhibitory concentration of compounds was determined as detailed previously (38) for *M. tuberculosis*. *C. glutamicum* minimal inhibitory concentrations were obtained by serial twofold dilution on 96-well plates which were incubated at 30 °C and read after 48 h (19).

SPR Details. SPR assays were carried out as we previously published (38), all SPR experiments were carried out on a BIAcore T200 instrument, and all analysis was performed using BIAevaluate.

Reconstitution Details and Assays. Reconstitution of MmpL3tb, MmpL3ΔCtb, and CmpL1 and their TEV site-containing variants was carried out as described before, with the following modifications (39, 40): 50 μg of eluted MmpL3tb was mixed with 4 mg of dispersed lipids, and the volume was adjusted to 500 μL via addition of reconstitution buffer supplemented with 1.1% octyl β-D-glucopyranoside (40). The sample was incubated at room temperature for 10 min, then diluted slowly to 35 mL with prechilled reconstitution buffer and allowed to dialyze for 1 h at 4 °C with stirring against reconstitution buffer supplemented with SM-2 BioBeads (2 g/L) (60). The sample was then ultracentrifuged (Beckman 45Ti) at 35,000 rpm for 90 min, and the resulting pellet was resuspended in 200 μL of reconstitution buffer. Pyranine was added to the sample at a final concentration of 2 mM, and the sample was extruded first through a 400-nm, then a 200-nm pore (Avanti Mini Extruder). The sample was then passed through a PD-10 gel filtration column (GE Life Sciences) to remove untrapped pyranine. Control vesicles devoid of proteins were prepared in parallel by the addition of reconstitution buffer in lieu of protein. For reconstitution assays with substrate analogs, 50 nM substrate was incubated with vesicles for 5 min prior to their addition to buffers, data collection began immediately, and, unless otherwise indicated, inhibitor concentration in the 96 well plate was 50 nM.

Chemical materials, instrumentation, and synthesis are described in *SI Appendix*.

Molecular Dynamics Simulations. Details of MD simulations are provided in *SI Appendix*. The MmpL3smg model was created using the structure reported (PDB ID: 6AJF) (27).

To build the MmpL3smg trimer, we used the minimized structure from the previous step and aligned it with the AcrB structure (PDB ID: 1OY9) followed by replicating the MmpL3smg monomer using the transformation matrix for generating the AcrB trimer.

Data Availability. All study data are included in the article and/or supporting information.

ACKNOWLEDGMENTS. This work was supported by a grant from the NIH/National Institute of Allergy and Infectious Diseases (Grant AI116525) (to M.J., H.I.Z., J.N., and J.C.G). The content is solely the responsibility of the authors and does not necessarily represent the official views of the NIH. We are grateful to the Global Alliance for TB Drug Development for the provision of NITD-304 and NITD-349, to Dr. Remuinan-Blanco (GSK Tres Cantos Open Lab Foundation) for the provision of THPP1, to Dr. Lee (St. Jude Children's Research Hospital) for the provision of SQ109, and to Dr. Jacobs (Albert Einstein College of Medicine, NY) for *Mtb* H37Rv strain mc^{2}6206. SPR experiments were carried out using a Biacore T200 instrument of the Oklahoma Medical Research Foundation Biacore Facility, which is funded by the Shared Instrumentation Grant S10 OD025014. Computational resources were provided through the Extreme Science and Engineering Discovery Environment (Grant TG-MCB130173), which is supported by NSF Grant ACI-1548562. Y.L. and J.L. acknowledges Tang Aoqing Honors Program in Science, College of Chemistry, Jilin University, Changchun, Jilin Province, China.

Author affiliations: [a]Department of Chemistry and Biochemistry, University of Oklahoma, Norman, OK 73019; [b]School of Pharmacy & Health Professions, Department of Pharmacy Sciences, Creighton University, Omaha, NE 68178; [c]Mycobacteria Research Laboratories, Department of Microbiology, Immunology and Pathology, Colorado State University, Fort Collins, CO 80523; [d]College of Chemistry, Jilin University, 130012 Changchun, China; [e]Tang Aoqing Honors Program in Science, Jilin University, 130012 Changchun, China; and [f]School of Physics, Georgia Institute of Technology, Atlanta, GA 30332

Author contributions: J.C.G., J.N., M.J., and H.I.Z. designed research; C.M.S., S.O.B., A.N.P., W.L., Y.L., J.M., R.S., P.H., P.K.P., A.A., J.L., and J.C.G. performed research; J.N. contributed new reagents/analytic tools; J.C.G., M.J., and H.I.Z. analyzed data; and C.M.S., J.C.G., J.N., M.J., and H.I.Z. wrote the paper.

1. TDR, "Priorities for tuberculosis research: A report of the Disease reference group report on TB, leprosy and Buruli ulcer" (World Health Organization, 2013). ISBN 978 92 4 150597 0.
2. E. A. Barka *et al.*, Taxonomy, physiology, and natural products of actinobacteria. *Microbiol. Mol. Biol. Rev.* **80**, 1–43 (2015).
3. I. Smith, *Mycobacterium tuberculosis* pathogenesis and molecular determinants of virulence. *Clin. Microbiol. Rev.* **16**, 463–496 (2003).
4. M.-R. Lee *et al.*, *Mycobacterium abscessus* complex infections in humans. *Emerg. Infect. Dis.* **21**, 1638–1646 (2015).
5. R. Nessar, E. Cambau, J. M. Reyrat, A. Murray, B. Gicquel, *Mycobacterium abscessus*: A new antibiotic nightmare. *J. Antimicrob. Chemother.* **67**, 810–818 (2012).
6. Y. Fujikura *et al.*, A case of *Nocardia asteroides* infection in a patient with HIV/AIDS diagnosed by endobronchial ultrasound-guided transbronchial needle aspiration (EBUS-TBNA). *Intern. Med.* **51**, 1413–1417 (2012).
7. K. Bernard, The genus *Corynebacterium* and other medically relevant coryneform-like bacteria. *J. Clin. Microbiol.* **50**, 3152–3158 (2012).
8. H. Marrakchi, M. A. Lanéelle, M. Daffé, Mycolic acids: Structures, biosynthesis, and beyond. *Chem. Biol.* **21**, 67–85 (2014).
9. V. Nataraj *et al.*, Mycolic acids: Deciphering and targeting the Achilles' heel of the tubercle bacillus. *Mol. Microbiol.* **98**, 7–16 (2015).
10. K. M. Backus *et al.*, The three *Mycobacterium tuberculosis* antigen 85 isoforms have unique substrates and activities determined by non-active site regions. *J. Biol. Chem.* **289**, 25041–25053 (2014).
11. H. Nikaido, Prevention of drug access to bacterial targets: Permeability barriers and active efflux. *Science* **264**, 382–388 (1994).
12. R. Bansal-Mutalik, H. Nikaido, Mycobacterial outer membrane is a lipid bilayer and the inner membrane is unusually rich in diacyl phosphatidylinositol dimannosides. *Proc. Natl. Acad. Sci. U.S.A.* **111**, 4958–4963 (2014).
13. R. Bailo, A. Bhatt, J. A. Aínsa, Lipid transport in *Mycobacterium tuberculosis* and its implications in virulence and drug development. *Biochem. Pharmacol.* **96**, 159–167 (2015).
14. S. Gavalda *et al.*, The polyketide synthase Pks13 catalyzes a novel mechanism of lipid transfer in mycobacteria. *Chem. Biol.* **21**, 1660–1669 (2014).
15. D. Portevin *et al.*, A polyketide synthase catalyzes the last condensation step of mycolic acid biosynthesis in mycobacteria and related organisms. *Proc. Natl. Acad. Sci. U.S.A.* **101**, 314–319 (2004).
16. D. J. Lea-Smith *et al.*, The reductase that catalyzes mycolic motif synthesis is required for efficient attachment of mycolic acids to arabinogalactan. *J. Biol. Chem.* **282**, 11000–11008 (2007).
17. A. Bhatt, A. K. Brown, A. Singh, D. E. Minnikin, G. S. Besra, Loss of a mycobacterial gene encoding a reductase leads to an altered cell wall containing beta-oxo-mycolic acid analogs and accumulation of ketones. *Chem. Biol.* **15**, 930–939 (2008).
18. Y. Yamaryo-Botte *et al.*, Acetylation of trehalose mycolates is required for efficient MmpL-mediated membrane transport in Corynebacterineae. *ACS Chem. Biol.* **10**, 734–746 (2015).
19. L. Yang *et al.*, RND transporters protect *Corynebacterium glutamicum* from antibiotics by assembling the outer membrane. *MicrobiologyOpen* **3**, 484–496 (2014).
20. J. M. Belardinelli *et al.*, Structure-function profile of MmpL3, the essential mycolic acid transporter from *Mycobacterium tuberculosis*. *ACS Infect. Dis.* **2**, 702–713 (2016).
21. C. Varela *et al.*, MmpL genes are associated with mycolic acid metabolism in Mycobacteria and Corynebacteria. *Chem. Biol.* **19**, 498–506 (2012).
22. P. Domenech, M. B. Reed, C. E. Barry 3rd, Contribution of the *Mycobacterium tuberculosis* MmpL protein family to virulence and drug resistance. *Infect. Immun.* **73**, 3492–3501 (2005).
23. A. E. Grzegorzewicz *et al.*, Inhibition of mycolic acid transport across the *Mycobacterium tuberculosis* plasma membrane. *Nat. Chem. Biol.* **8**, 334–341 (2012).
24. Z. Xu, V. A. Meshcheryakov, G. Poce, S. S. Chng, MmpL3 is the flippase for mycolic acids in mycobacteria. *Proc. Natl. Acad. Sci. U.S.A.* **114**, 7993–7998 (2017).
25. C. Carel *et al.*, *Mycobacterium tuberculosis* proteins involved in mycolic acid synthesis and transport localize dynamically to the old growing pole and septum. *PLoS One* **9**, e97148 (2014).
26. J. M. Belardinelli *et al.*, The MmpL3 interactome reveals a complex crosstalk between cell envelope biosynthesis and cell elongation and division in mycobacteria. *Sci. Rep.* **9**, 10728 (2019).
27. C. C. Su *et al.*, MmpL3 is a lipid transporter that binds trehalose monomycolate and phosphatidylethanolamine. *Proc. Natl. Acad. Sci. U.S.A.* **116**, 11241–11246 (2019).
28. B. Zhang *et al.*, Crystal structures of membrane transporter MmpL3, an anti-TB Drug target. *Cell* **176**, 636–648.e13 (2019).
29. O. Adams *et al.*; CRyPTIC Consortium, Cryo-EM structure and resistance landscape of *M. tuberculosis* MmpL3: An emergent therapeutic target. *Structure* **29**, 1182–1191.e4 (2021).
30. N. D. Franz *et al.*, Design, synthesis and evaluation of indole-2-carboxamides with pan anti-mycobacterial activity. *Bioorg. Med. Chem.* **25**, 3746–3755 (2017).
31. W. Li *et al.*, Synergistic interactions of MmpL3 inhibitors with antitubercular compounds *in vitro*. *Antimicrob. Agents Chemother.* **61**, e02399-16 (2017).
32. G. Degiacomi *et al.*, Essentiality of mmpL3 and impact of its silencing on *Mycobacterium tuberculosis* gene expression. *Sci. Rep.* **7**, 43495 (2017).
33. W. Li *et al.*, Therapeutic potential of the *Mycobacterium tuberculosis* mycolic acid transporter, MmpL3. *Antimicrob. Agents Chemother.* **60**, 5198–5207 (2016).
34. S. Lun *et al.*, Indoleamides are active against drug-resistant *Mycobacterium tuberculosis*. *Nat. Commun.* **4**, 2907 (2013).
35. K. A. Sacksteder, M. Protopopova, C. E. Barry 3rd, K. Andries, C. A. Nacy, Discovery and development of SQ109: A new antitubercular drug with a novel mechanism of action. *Future Microbiol.* **7**, 823–837 (2012).
36. D. Deidda *et al.*, Bactericidal activities of the pyrrole derivative BM212 against multidrug-resistant and intramacrophagic *Mycobacterium tuberculosis* strains. *Antimicrob. Agents Chemother.* **42**, 3035–3037 (1998).
37. W. Li *et al.*, MmpL3 as a target for the treatment of drug-resistant nontuberculous mycobacterial infections. *Front. Microbiol.* **9**, 1547 (2018).
38. W. Li *et al.*, Direct inhibition of MmpL3 by novel antitubercular compounds. *ACS Infect. Dis.* **5**, 1001–1012 (2019).
39. H. I. Zgurskaya, H. Nikaido, Bypassing the periplasm: Reconstitution of the AcrAB multidrug efflux pump of *Escherichia coli*. *Proc. Natl. Acad. Sci. U.S.A.* **96**, 7190–7195 (1999).
40. M. Picard *et al.*, "Biochemical reconstitution and characterization of multicomponent drug efflux transporters" in *Bacterial Multidrug Exporters: Methods and Protocols*, A. Yamaguchi, K. Nishino, Eds. (Springer, New York, NY, 2018), pp. 113–145.
41. K. Yamamoto, N. Nakata, T. Mukai, I. Kawagishi, M. Ato, Coexpression of MmpS5 and MmpL5 contributes to both efflux transporter MmpL5 trimerization and drug resistance in *Mycobacterium tuberculosis*. *MSphere* **6**, e00518-20 (2021).
42. K. Tahlan *et al.*, SQ109 targets MmpL3, a membrane transporter of trehalose monomycolate involved in mycolic acid donation to the cell wall core of *Mycobacterium tuberculosis*. *Antimicrob. Agents Chemother.* **56**, 1797–1809 (2012).
43. M. J. Remuiñán *et al.*, Tetrahydropyrazolo[1,5-a]pyrimidine-3-carboxamide and N-benzyl-6′,7′-dihydrospiro[piperidine-4,4′-thieno[3,2-c]pyran] analogues with bactericidal efficacy against *Mycobacterium tuberculosis* targeting MmpL3. *PLoS One* **8**, e60933 (2013).

44. V. La Rosa *et al.*, MmpL3 is the cellular target of the antitubercular pyrrole derivative BM212. *Antimicrob. Agents Chemother.* **56**, 324–331 (2012).
45. S. P. Rao *et al.*, Indolcarboxamide is a preclinical candidate for treating multidrug-resistant tuberculosis. *Sci. Transl. Med.* **5**, 214ra168 (2013).
46. A. N. Pandya, E. M. Villa, E. J. North, A simple and efficient approach for the synthesis of 2-aminated quinazoline derivatives via metal free oxidative annulation. *Tetrahedron Lett.* **58**, 1276–1279 (2017).
47. R. R. Kondreddi *et al.*, Design, synthesis, and biological evaluation of indole-2-carboxamides: A promising class of antituberculosis agents. *J. Med. Chem.* **56**, 8849–8859 (2013).
48. A. P. Kozikowski *et al.*, Targeting mycolic acid transport by indole-2-carboxamides for the treatment of *Mycobacterium abscessus* infections. *J. Med. Chem.* **60**, 5876–5888 (2017).
49. O. K. Onajole *et al.*, Preliminary structure-activity relationships and biological evaluation of novel antitubercular indolecarboxamide derivatives against drug-susceptible and drug-resistant *Mycobacterium tuberculosis* strains. *J. Med. Chem.* **56**, 4093–4103 (2013).
50. A. N. Pandya *et al.*, Indole-2-carboxamides are active against *Mycobacterium abscessus* in a mouse model of acute infection. *Antimicrob. Agents Chemother.* **63**, e02245-18 (2019).
51. J. Stec *et al.*, Indole-2-carboxamide-based MmpL3 inhibitors show exceptional antitubercular activity in an animal model of tuberculosis infection. *J. Med. Chem.* **59**, 6232–6247 (2016).
52. W. Li *et al.*, Novel insights into the mechanism of inhibition of MmpL3, a target of multiple pharmacophores in *Mycobacterium tuberculosis*. *Antimicrob. Agents Chemother.* **58**, 6413–6423 (2014).
53. K. Li *et al.*, Multitarget drug discovery for tuberculosis and other infectious diseases. *J. Med. Chem.* **57**, 3126–3139 (2014).
54. X. Feng *et al.*, Antiinfectives targeting enzymes and the proton motive force. *Proc. Natl. Acad. Sci. U.S.A.* **112**, E7073–E7082 (2015).
55. M. H. Foss *et al.*, Diphenylether-modified 1,2-diamines with improved drug properties for development against *Mycobacterium tuberculosis*. *ACS Infect. Dis.* **2**, 500–508 (2016).
56. A. Viljoen *et al.*, The diverse family of MmpL transporters in mycobacteria: From regulation to antimicrobial developments. *Mol. Microbiol.* **104**, 889–904 (2017).
57. T. Eicher *et al.*, Coupling of remote alternating-access transport mechanisms for protons and substrates in the multidrug efflux pump AcrB. *eLife* **3**, e03145 (2014).
58. A. Yamaguchi, R. Nakashima, K. Sakurai, Structural basis of RND-type multidrug exporters. *Front. Microbiol.* **6**, 327 (2015).
59. M. Zwama *et al.*, Multiple entry pathways within the efflux transporter AcrB contribute to multidrug recognition. *Nat. Commun.* **9**, 124 (2018).
60. J.-L. Rigaud, D. Lévy, "Reconstitution of Membrane Proteins into Liposomes" in *Liposomes, Part B*, N. Duzgunes, Ed. (*Methods in Enzymology*, Academic, 2003), **vol. 372**, pp. 65–86.